

# The effect of cobalt and boron on the structural, microstructural, and optoelectronic properties of ZnO nanoparticles

S.D. Senol<sup>a</sup>, E. Ozugurlu<sup>b</sup>, L. Arda<sup>c,\*</sup>

<sup>a</sup> Bolu Abant İzzet Baysal University, Department of Chemistry, 14280, Bolu, Turkey

<sup>b</sup> Istanbul Technical University, Department of Mathematics, 34469, Maslak, Istanbul, Turkey

<sup>c</sup> Bahcesehir University, Faculty of Engineering and Natural Sciences, Department of Mechatronic Engineering, 34349, Besiktas, Istanbul, Turkey



## ARTICLE INFO

### Keywords:

Zinc oxide  
Nanoparticles  
Energy gap  
Refractive index  
Urbach energy

## ABSTRACT

Co/B co-doped ZnO ( $\text{Zn}_{0.93-x}\text{Co}_x\text{B}_{0.07}\text{O}$ ,  $x = 0.00, 0.01, 0.02, 0.03, 0.04, \text{ and } 0.05$ ) nanoparticles were synthesized by the hydrothermal method to investigate the effect of cobalt and boron on the structural, microstructural, and optoelectronic properties of ZnO nanoparticles. The X-ray diffraction method was used for the structural analysis and single phases were found for all Co/B co-doped ZnO nanoparticles. Scanning Electron Microscope (SEM) technique was used to determine the surface morphology, particle size, and the shapes of the nanoparticles. The elemental compositions of the nanoparticles were obtained by electron dispersive spectroscopy (EDS). Hexagonal Wurtzite structure was proved by  $c/a$  ratios of the ZnCoBO nanoparticles. The Fourier transform infrared (FTIR) studies were performed and explained. The energy band gaps of the samples were calculated and the effects of dopant elements on optical properties were discussed. The maximum band gap occurred for  $\text{Zn}_{0.93}\text{B}_{0.07}\text{O}$  with a band gap energy of  $E_g = 3.26$  eV. The refractive index was calculated using the energy band gap with five different models. The grain sizes and the band gap energies fluctuated as the doping ratio increased. The results showed that the refractive index strongly depends on the Co concentration non-linearly. It was found that doping cobalt increased the Urbach energy value of B-doped ZnO nanoparticles. The increase in  $E_u$  indicates that the structural disorder and the number of defects in the  $\text{Zn}_{0.93-x}\text{Co}_x\text{B}_{0.07}\text{O}$  structures increased with increasing concentration of Co in the  $\text{Zn}_{0.93-x}\text{Co}_x\text{B}_{0.07}\text{O}$  structures. The highest value of Urbach energy was approximately found in the range of 1259 and 1469 meV for 3% Co. Moreover, for 3% Co the concentration-dependent microstrain ( $\epsilon$ ) values also reached the maximum, dislocation density  $\delta$  had also the maximum value.

## 1. Introduction

Optoelectronic and sensor industries require materials with the properties of high refractive index  $n$  and wide band gap  $E_g$  since both properties increase the performance of optical interference filters and optical sensors. In 2019, Naccarato et al. [1] reported that how the relation between the high refraction index and band gap was effected by the chemistry and why certain classes of materials among 4000 semiconductors would perform better. They reviewed some of the refractive index calculation models based on band gap values. These models are Ravindra et al. [2], Moss [3], Hervé and Vandamme [4], Reddy and Anjayenulu [5], and Kumar and Singh [6].

Zinc oxide (ZnO) is a good candidate for functional components of devices and materials in photonic crystals [7,8], spintronics [9], gas sensors [10], light-emitting diodes [11,12], microelectronics, solar cells

[13], lasers [14], varistors [15] and photoelectrochemical cells [16]. Moreover, ZnO is also one of the important and emerging semiconductor materials with the direct band gap of  $\sim 3.37$  eV [9] and a large exciton binding energy of  $\sim 60$  meV [17] at room temperature (RT).

It is crucial to decide which element or elements must be doped into ZnO to control the band gap, electrical conductivity, and increase the carrier concentration. In the last decades, many articles have been published on the doping of transition metals (TMs) such as Co, Cr, Cu, Er, Fe, Mg, Mn, Ni, and Tb into ZnO due to the potential applications [18–29].

Since Co atoms have a radius (0.65 Å) and electronic shell similar to those of Zn atoms (0.74 Å), the lattice constant does not change when zinc oxide is doped by Co.

Thus, many researchers have been studying heavily the effects of Co doping on the optoelectronic properties and magnetism of ZnO films

\* Corresponding author. Ciragan Cad, Osmanpasa Mektebi Sok, 34349, Besiktas, Istanbul, Turkey  
E-mail address: [lutfi.arda@eng.bau.edu.tr](mailto:lutfi.arda@eng.bau.edu.tr) (L. Arda).

<https://doi.org/10.1016/j.ceramint.2019.11.193>

Received 1 November 2019; Received in revised form 21 November 2019; Accepted 21 November 2019

Available online 23 November 2019

0272-8842/ © 2019 Elsevier Ltd and Techna Group S.r.l. All rights reserved.

which are prepared by hydrothermal method, pulsed laser deposition, sol-gel processes, magnetron RF sputtering, magnetron DC sputtering, and spray pyrolysis [30–37]. Several studies indicate that the addition of Co in ZnO increases the ferromagnetic moment [35].

Recently, as a good conductor, non-toxic, low cost, and easily available material, Boron has been chosen as dopant [38–43]. In addition, to improve the electronic conductivity, the n-type metal oxide is produced upon doping metal oxide with boron. Moreover, it was shown that the properties of thermal stability were improved by the addition of B in ZnO films [44–47].

According to the findings of Senol et al. [41], the impurity scattering mechanism was more dominant in the range of 0–7% B content region; thus, in this paper, the boron concentration was taken as 7%. In order to have lower resistivity and broader optical band gap, deposited or annealed B-doped ZnO films were preferred to pure ZnO film [48,49]. Since boron has a small ion radius (0.23 Å), it can act as either interstitial boron or substituted one in ZnO lattice [45,48,49]. However, excessive doping can damage the crystal quality. Thus, it is important to investigate how much doping must be added.

According to Pawar et al. [49], the  $B_n$ ZnO electrodes could be used instead of indium- or fluorine-doped tin oxide as a substrate.

In 2013, Kim et al. [50] reported that BZO nanorods can help to improve photonic and optoelectronic devices since a red-shift of the emission energies occurred when the temperature was increased. Moreover,  $B^{3+}$  has a remarkably higher Lewis acid strength (10.7) than that of  $Al^{3+}$  (3.04) [51]. In addition, Jana et al. also reported that boron doping could improve the physical properties of ZnO thin films [52].

In this study,  $Zn_{0.93-x}Co_xB_{0.07}O$  nanoparticles were synthesized using the hydrothermal method by varying the dopant ratio from  $x = 0.01$  to 0.05 with an increment of 0.01. The structural and optoelectronic properties such as refractive index, band gap and reflectance spectra of the samples were calculated by using five different models, namely, Ravindra et al. [2], Moss [3], Hervé and Vandamme [4], Reddy and Anjayenulu [5], Kumar and Singh [6]. The Urbach energy values were calculated using finite difference methods.

## 2. Experimental procedure

### 2.1. Preparation of $Zn_{0.93-x}Co_xB_{0.07}O$ nanoparticles

$Zn_{0.93-x}Co_xB_{0.07}O$  ( $x = 0.00, 0.01, 0.02, 0.03, 0.04, 0.05$ ) powders were synthesized using hydrothermal synthesis process by highly pure chemicals (> 99% purity) Zinc acetate dehydrate ( $Zn(CH_3CO_2)_2 \cdot 2H_2O$ ), cobalt(II)acetate tetrahydrate ( $Co(CH_3CO_2)_2 \cdot 4H_2O$ ), boric acid ( $H_3BO_3$ ), and hexamethylenetetramine (HMT). Aqueous solutions in equal molarities were prepared by means of magnetic stirring for 10 min using appropriate amounts of zinc acetate, boric acid, and HMT. Then,  $Co(CH_3CO_2)_2 \cdot 4H_2O$  was poured into the solution and stirred for 2 h to yield a clear and homogeneous solution at room temperature. These solutions were kept into the Teflon-lined autoclave. During 12 h and using an electric oven, the reaction was conducted at 95 °C. Then at room temperature, the as-formed precipitates were filtered, washed by distilled water and dried in air. The calcination procedure was applied to the dried powders for 2 h at 750 °C under air atmosphere and followed by furnace cooling as shown in (Fig. 1).

### 2.2. Characterization techniques

The phase study of  $Zn_{0.93-x}Co_xB_{0.07}O$  ( $x = 0.0, 0.01, 0.02, 0.03, 0.04, 0.05$ ) nanoparticles were done by powder X-ray diffraction. XRD patterns were obtained by means of Rigaku Multiflex diffractometer using  $Cu K\alpha$  radiation ( $\lambda = 1.5408 \text{ \AA}$ ), in the scan range of  $2\theta$  between 20° and 80° with a scan speed of 3°/min and with a step increment of 0.02. To detail the optical properties of the samples, double beam Shimadzu 2600 UV-spectrometer was used with an integrating sphere

in the wavelength range of 200–900 nm. By the PerkinElmer Spectrum Two FTIR-ATR spectrophotometer, the Fourier transform infrared (FTIR) spectra of all samples were recorded in the range of 4000–400  $cm^{-1}$ .

## 3. Results and discussions

### 3.1. Structural characterization

The powder patterns of all  $Zn_{0.93-x}Co_xB_{0.07}O$  ( $x = 0.0, 0.01, 0.02, 0.03, 0.04, 0.05$ ) nanoparticles were obtained in the range of  $20^\circ \leq 2\theta \leq 80^\circ$  and shown in Fig. 2. The peak position of all Co-doped samples presented no variation when compared with  $Zn_{0.93}B_{0.07}O$  sample and the highest peak was indexed as (101), this means that ZnO nanoparticles had a preferential crystallographic (101) orientation. Moreover, as seen in all XRD patterns, there is no observed secondary peak and this is the indication of the quality of sample preparation. The concentration-dependent particle sizes, lattice parameters, volume of the unit cell, microstrain ( $\epsilon$ ), stress ( $\sigma$ ), dislocation density ( $\delta$ ) (the amount of defect in the sample), the locality of the atoms and their displacement ( $u$ ), and bond length  $L$  were calculated and listed in Tables 1 and 2 using XRD analysis of all samples. The detailed evaluations of  $\epsilon$ ,  $\sigma$ ,  $\delta$ ,  $D$ ,  $u$ ,  $V$ , and  $L$  parameters were given below. ZnO bond length is calculated by the following equation [18,19];

$$L = \sqrt{\left(\frac{a^2}{3}\right) + [0.5 - u]^2 c^2}$$

where  $a$  and  $c$  are lattice constants of ZnO and  $u$  is the wurtzite structure which can be found as;

$$u = \left(\frac{a^2}{3c^2}\right) + 0.25$$

The lattice constants  $a$  and  $c$  are calculated with the following formula [18,19]:

$$\frac{1}{d_{hkl}^2} = \frac{4}{3} \left( \frac{h^2 + hk + k^2}{a^2} \right) + \frac{l^2}{c^2}$$

The particle size was calculated from the XRD peak width of (101) based on the Debye–Scherrer equation [18],

$$D = \frac{K \lambda}{\beta_{hkl} \cos(\theta)}$$

where  $\beta_{hkl}$  is the integral half-width,  $K$  is a constant equal to 0.90,  $\lambda$  is the wavelength of the incident X-ray ( $\lambda = 0.1540 \text{ nm}$ ),  $D$  is the particle size, and  $\theta$  is the Bragg angle.

The particle size calculated for synthesized ZnO nanoparticles was in the range of 22.95–26.43 nm.

Figs. 3–5 were presented to figure out the behavior of microstrain ( $\epsilon$ ), stress ( $\sigma$ ) (given in Table 1) in different Co concentrations in  $Zn_{0.93-x}Co_xB_{0.07}O$  for  $x = 0.00, 0.01, 0.02, 0.03, 0.04$ , and 0.05. As can be seen from Table 1, the lattice parameters  $a$  and  $c$  are slightly the same which means that there is no any change in the crystal structure by Co-content, in agreement with the literature [28].

It is known that in an ideal wurtzite structure  $c/a = \sqrt{8/3} = 1.633$ , however, our experimentally observed  $c/a$  ratios (in the range of 1.602–1.603) are smaller than ideal; this is probably due to lattice stability. The maximum values in  $c/a$ , unit cell volume and bond length ( $L$ ) were obtained in undoped  $Zn_{0.93}B_{0.07}O$  sample. In addition, as seen in Table 1, the  $c/a$  values did not change and they were in the range of 1.602–1.603 which showed that the obtained structure had a good quality.

As seen in Table 2, concentration-dependent microstrain ( $\epsilon$ ) and dislocation density  $\delta$  values reached to the maximum at the concentration rate of  $x = 0.03$  for  $Zn_{0.90}Co_{0.03}B_{0.07}O$  sample. The stress ( $\sigma$ ) and bond lengths were maximum and minimum at 2% Co

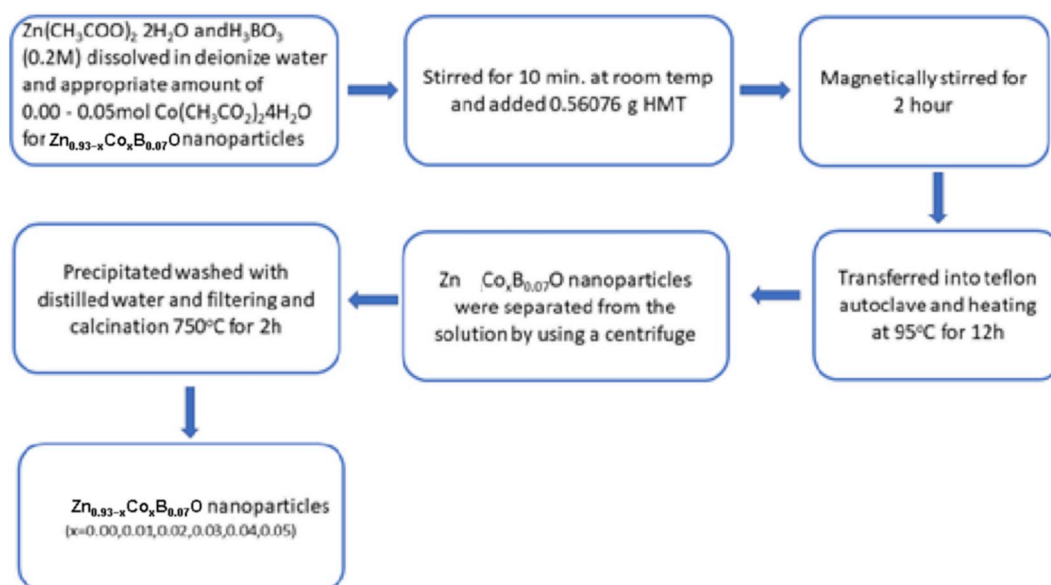


Fig. 1. Flow-chart showing the procedure of preparing the  $Zn_{0.93-x}Co_xB_{0.07}O$  ( $x = 0.0, 0.01, 0.02, 0.03, 0.04, 0.05$ ) nanoparticles.

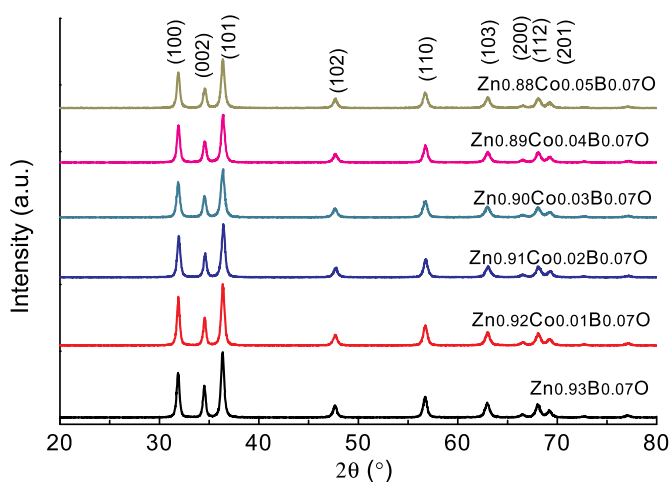


Fig. 2. The powder XRD patterns of all  $Zn_{0.93-x}Co_xB_{0.07}O$  ( $x = 0.0, 0.01, 0.02, 0.03, 0.04, 0.05$ ) nanoparticles prepared by hydrothermal method.

**Table 1**  
Concentration-dependent particle sizes, lattice parameters, atomic packing factor ( $c/a$ ) and volume of the unit cell.

Sample Name	D (nm)	a(Å)	c(Å)	c/a	Volume, V (Å <sup>3</sup> )
$Zn_{0.93}B_{0.07}O$	26.00	3.240	5.192	1.602	46.873
$Zn_{0.92}Co_{0.01}B_{0.07}O$	26.43	3.236	5.188	1.603	46.721
$Zn_{0.91}Co_{0.02}B_{0.07}O$	25.42	3.232	5.180	1.602	46.534
$Zn_{0.90}Co_{0.03}B_{0.07}O$	22.95	3.237	5.190	1.603	46.768
$Zn_{0.89}Co_{0.04}B_{0.07}O$	25.06	3.235	5.186	1.603	46.674
$Zn_{0.88}Co_{0.05}B_{0.07}O$	24.74	3.236	5.186	1.602	46.703

concentration, respectively. Table 2, Figs. 3 and 5 depicted that the stress ( $\sigma$ ) values were negative, a sign of compressive stress. Since none of the stress ( $\sigma$ ) values had a positive sign, there was no tensile stress in the structures. The atomic locality and their displacements exhibited almost stable behavior (without variation) with the increment of Co concentrations in the samples so we conclude that increasing the amount of Co rates in the structure does not affect the locality of atoms in the structure. As seen in Table 2, and bond length ( $L$ ) in  $Zn_{0.93-x}Co_xB_{0.07}O$  structures presented the maximum and minimum values at  $x = 0.00$  and  $x = 0.02$  concentration rates,

**Table 2**

The varying of concentration-dependent microstrain ( $\epsilon$ ), stress ( $\sigma$ ), dislocation density ( $\delta$ ) (the amount of defect in the sample), the locality of the atoms and their displacement ( $u$ ), and bond length ( $L$ ) in  $Zn_{0.93-x}Co_xB_{0.07}O$  structures.

Sample Name	$\epsilon$	$\sigma^*10^9$ (N/m <sup>2</sup> )	$\delta$ (nm <sup>-2</sup> )	$u$	$L$ (Å)	$E_g$
$Zn_{0.93}B_{0.07}O$	0.091	-1.132	$1.479 \times 10^{-3}$	0.380	1.972	3.257
$Zn_{0.92}Co_{0.01}B_{0.07}O$	0.094	-1.481	$1.431 \times 10^{-3}$	0.380	1.971	3.243
$Zn_{0.91}Co_{0.02}B_{0.07}O$	0.097	-2.178	$1.547 \times 10^{-3}$	0.380	1.967	3.229
$Zn_{0.90}Co_{0.03}B_{0.07}O$	0.107	-1.307	$1.898 \times 10^{-3}$	0.380	1.971	3.217
$Zn_{0.89}Co_{0.04}B_{0.07}O$	0.096	-1.655	$1.592 \times 10^{-3}$	0.380	1.969	3.247
$Zn_{0.88}Co_{0.05}B_{0.07}O$	0.097	-1.655	$1.633 \times 10^{-3}$	0.380	1.970	3.204

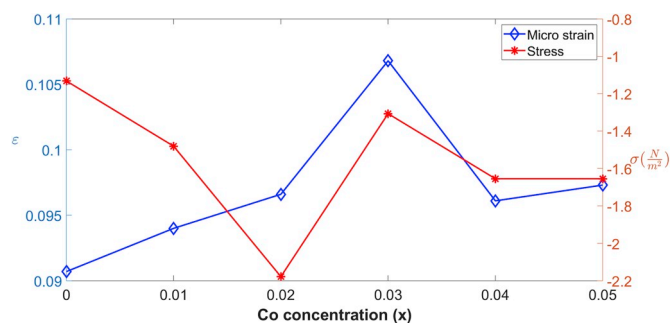


Fig. 3. Concentration-dependent microstrain ( $\epsilon$ ) and stress ( $\sigma$ ) values in  $Zn_{0.93-x}Co_xB_{0.07}O$  structures ( $x = 0.00, 0.01, 0.02, 0.03, 0.04, 0.05$ ).

respectively.

### 3.2. The morphology characteristics of $Zn_{0.93-x}Co_xB_{0.07}O$ nanoparticles

The morphology of all  $Zn_{0.93-x}Co_xB_{0.07}O$  nanoparticles was studied by the SEM technique in the range 1 and 2  $\mu m$  magnifications. As seen in Figs. 6–11, the particle distribution is random and is dominated by particle agglomeration. Moreover, all the SEM images showed the same pattern. The mapping and elemental composition of all  $Zn_{0.93-x}Co_xB_{0.07}O$  nanoparticles were provided by EDX analysis exhibited in Figs. 6 b-c, Figs. 7 b-c, Figs. 8 b-c, Figs. 9 b-c, Figs. 10 b-c, and Figs. 11 b-c. All peaks in EDX analysis belong to the intended composition without any other unwanted extra elemental peak contributions.

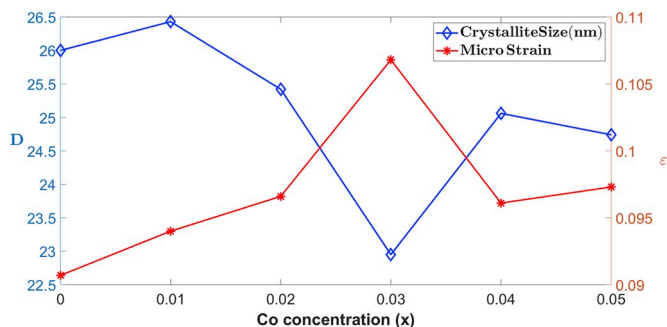


Fig. 4. Concentration-dependent particle size (*D*) values and microstrain ( $\epsilon$ ) variation in  $Zn_{0.93-x}Co_xB_{0.07}O$  structures ( $x = 0.00, 0.01, 0.02, 0.03, 0.04, 0.05$ ).

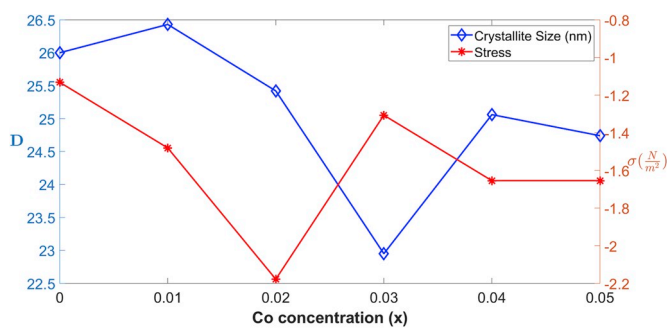


Fig. 5. Concentration-dependent particle size (*D*) values and stress ( $\sigma$ ) variation in.

### 3.3. The Fourier transform infrared (FTIR) studies

The band positions and the number of absorption peaks depend on chemical composition, morphology, and on the crystalline structure [53]. The ZnO infrared band values obtained by different methods vary in the literature [29,33,54,55]. According to Kansal et al. synthesized ZnO nanoparticles by means of the hydrothermal procedure and the corresponding FT-IR spectrum displayed an IR band positioned at  $478\text{ cm}^{-1}$  [56].

The obtained typical FTIR spectra of  $Zn_{0.93-x}Co_xB_{0.07}O$  nanoparticles for Co = 0%, 1%, 2%, 3%, 4%, and 5% are shown in Fig. 12. The obtained peak at  $509\text{ cm}^{-1}$  is assigned to Zn–O stretching frequency for  $Zn_{0.93}B_{0.07}O$  without Co concentration which shifted to  $496\text{ cm}^{-1}$  for  $Zn_{0.92}Co_{0.01}B_{0.07}O$ ;  $489\text{ cm}^{-1}$  for  $Zn_{0.91}Co_{0.02}B_{0.07}O$ ;  $496$  for  $Zn_{0.90}Co_{0.03}B_{0.07}O$ ; for  $Zn_{0.89}Co_{0.04}B_{0.07}O$   $496\text{ cm}^{-1}$ ; and for  $Zn_{0.88}Co_{0.05}B_{0.07}O$   $502\text{ cm}^{-1}$ . The absorption peaks observed between  $2300$  and  $2400\text{ cm}^{-1}$  is due to the existence of  $CO_2$  molecule in air. There is no absorption band for water absorbed on the ZnO surface. Also, the FTIR spectra do not reveal any band for CoO and  $CoO_4$ . The change in the characteristic frequency for Co–O and Zn–O bands reflects that the Zn–O–B network is perturbed by the presence of Co in its environment.

### 3.4. Optical properties

In analyzing the optical properties of semiconducting nanoparticles, UV-diffuse reflectance spectroscopy (UV-DRS) is one of the useful techniques. The reflectance is expected to depend on factors like oxygen deficiency, the band gap, impurity centers, and surface roughness. Fig. 13 depicts wavelength-dependent the UV-diffuse reflectance spectra of synthesized  $Zn_{0.93-x}Co_xB_{0.07}O$  nanoparticles using different Co doping in the range of  $300\text{--}700\text{ nm}$ .

In the visible light region, increasing Co doping gave rise to decrease the reflectance intensity. The absorption of  $Zn_{0.93}B_{0.07}O$

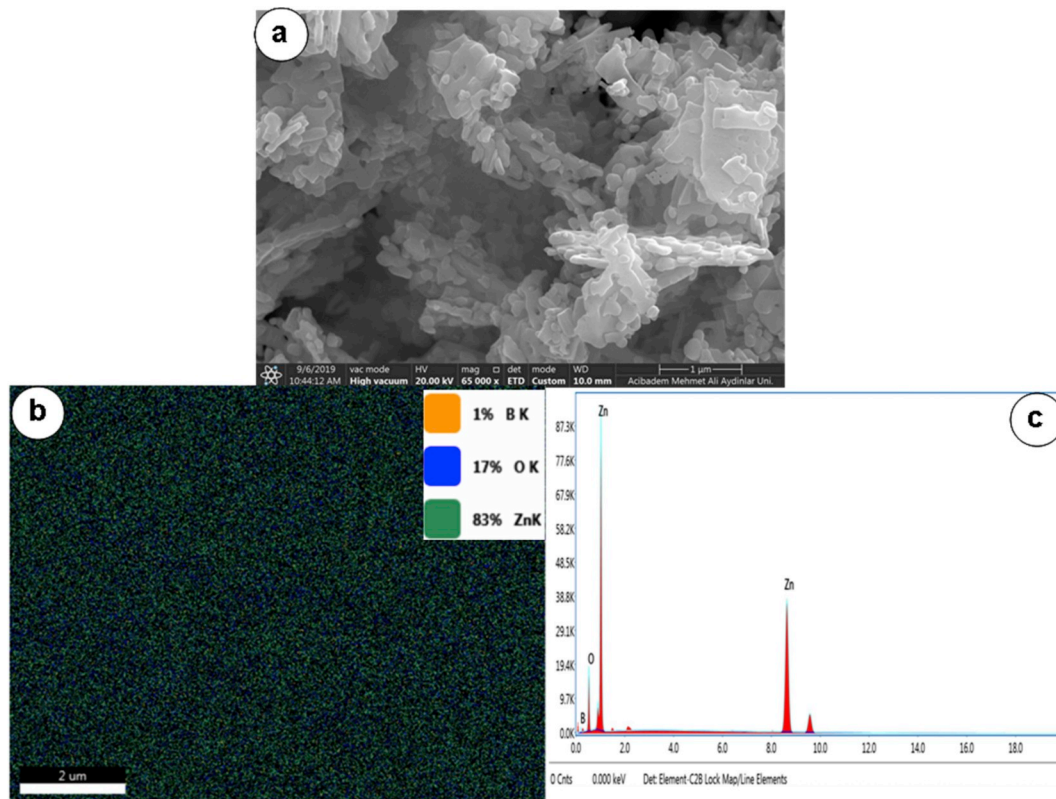


Fig. 6. SEM images of  $Zn_{0.93}B_{0.07}O$  composition for  $1\text{ }\mu\text{m}$  (a), the EDX mapping images (b), and the EDX graph of  $Zn_{0.93}B_{0.07}O$  sample in (c).

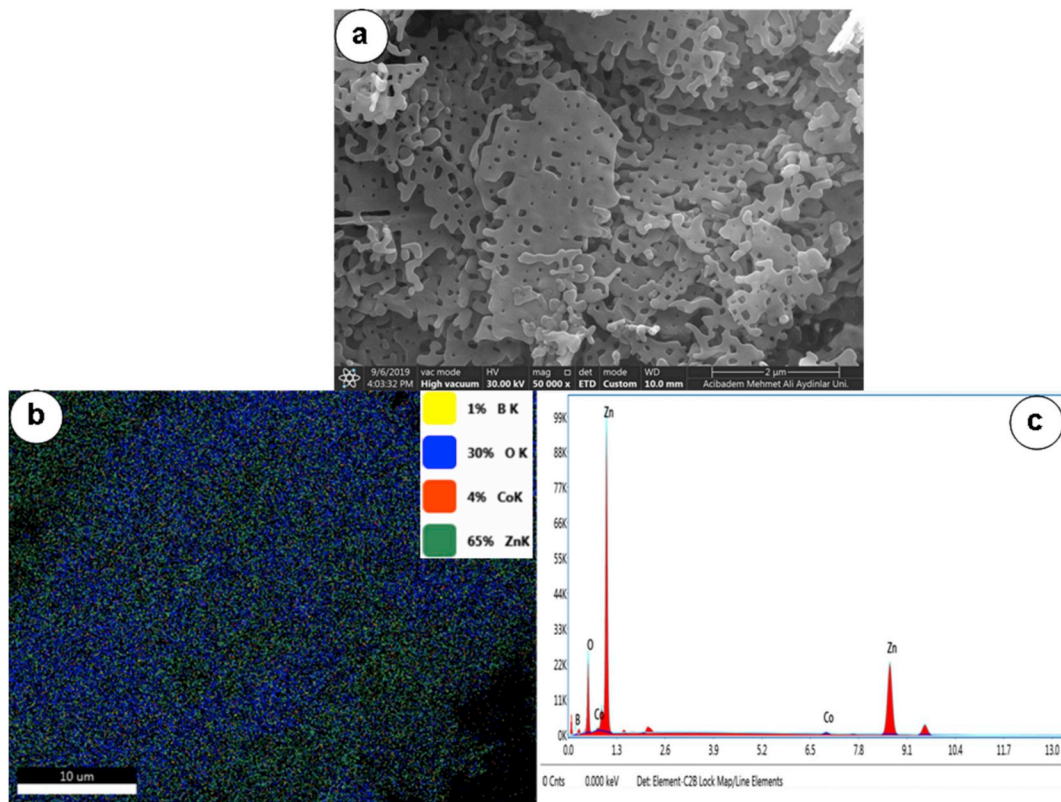


Fig. 7. SEM images of  $Zn_{0.92}Co_{0.01}B_{0.07}O$  composition for 2  $\mu m$  (a), the EDX mapping images (b), and the EDX graph of  $Zn_{0.92}Co_{0.01}B_{0.07}O$  sample in (c).

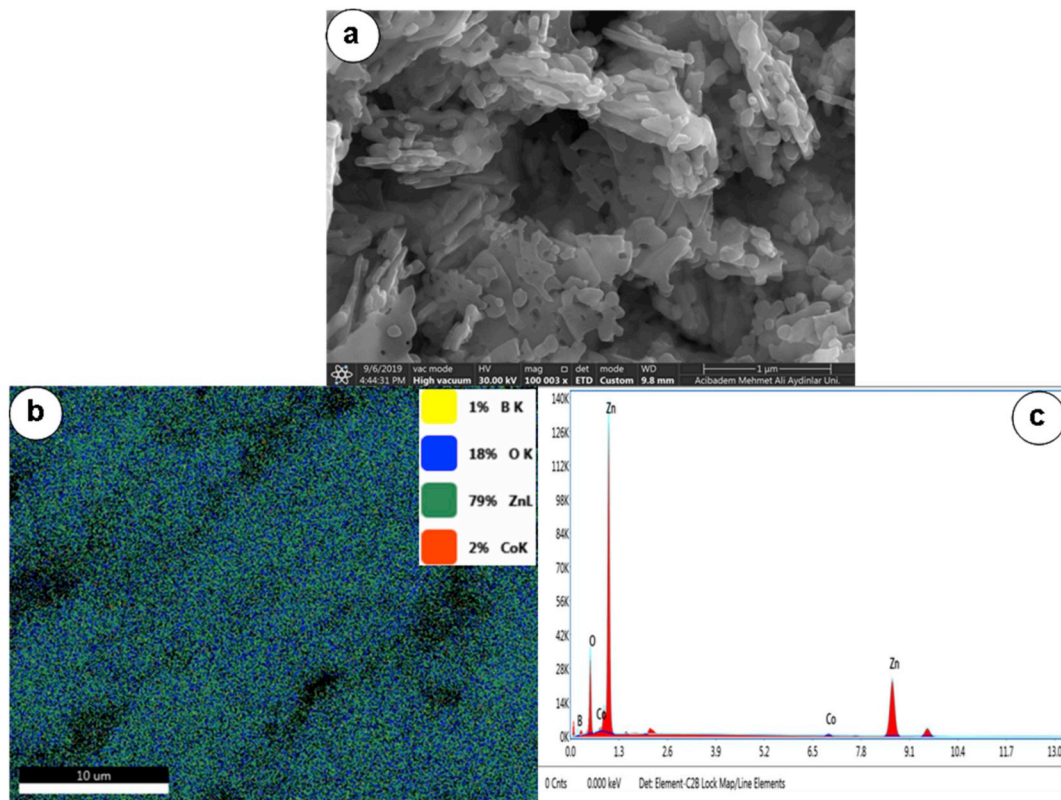


Fig. 8. SEM images of  $Zn_{0.91}Co_{0.02}B_{0.07}O$  composition for 1  $\mu m$  (a), the EDX mapping images (b), and the EDX graph of  $Zn_{0.91}Co_{0.02}B_{0.07}O$  sample in (c).

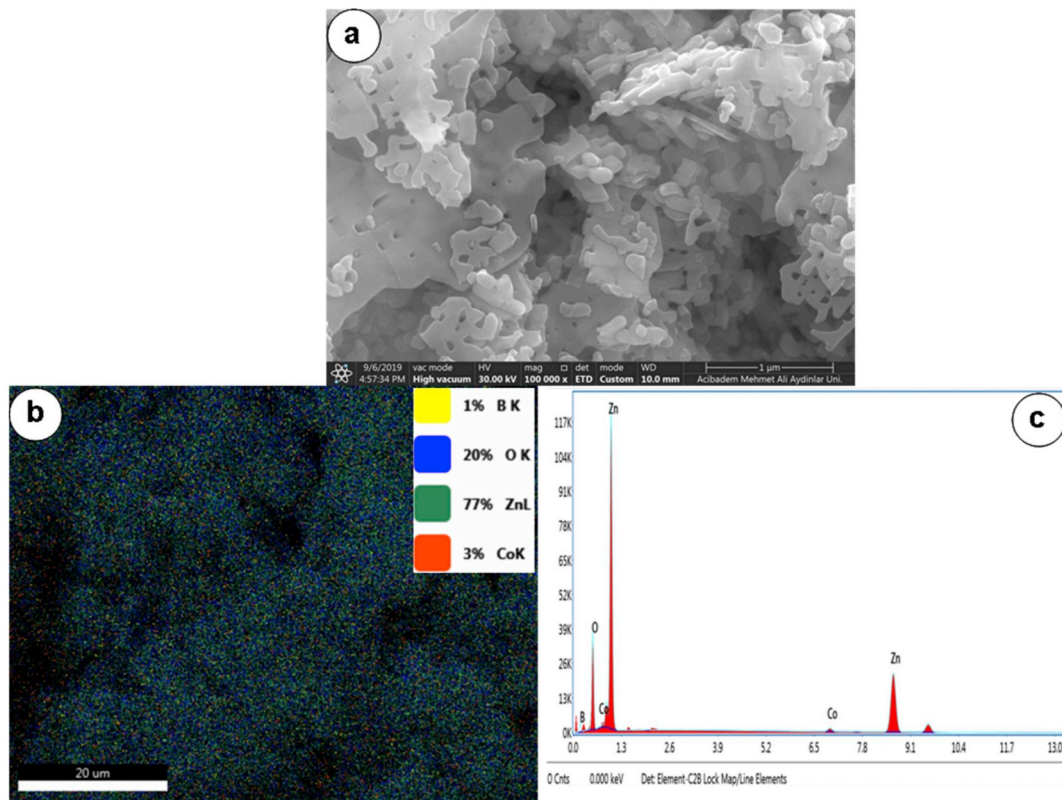


Fig. 9. SEM images of  $Zn_{0.90}Co_{0.03}B_{0.07}O$  composition for 1  $\mu m$  (a), the EDX mapping images (b), and the EDX graph of  $Zn_{0.90}Co_{0.03}B_{0.07}O$  sample in (c).

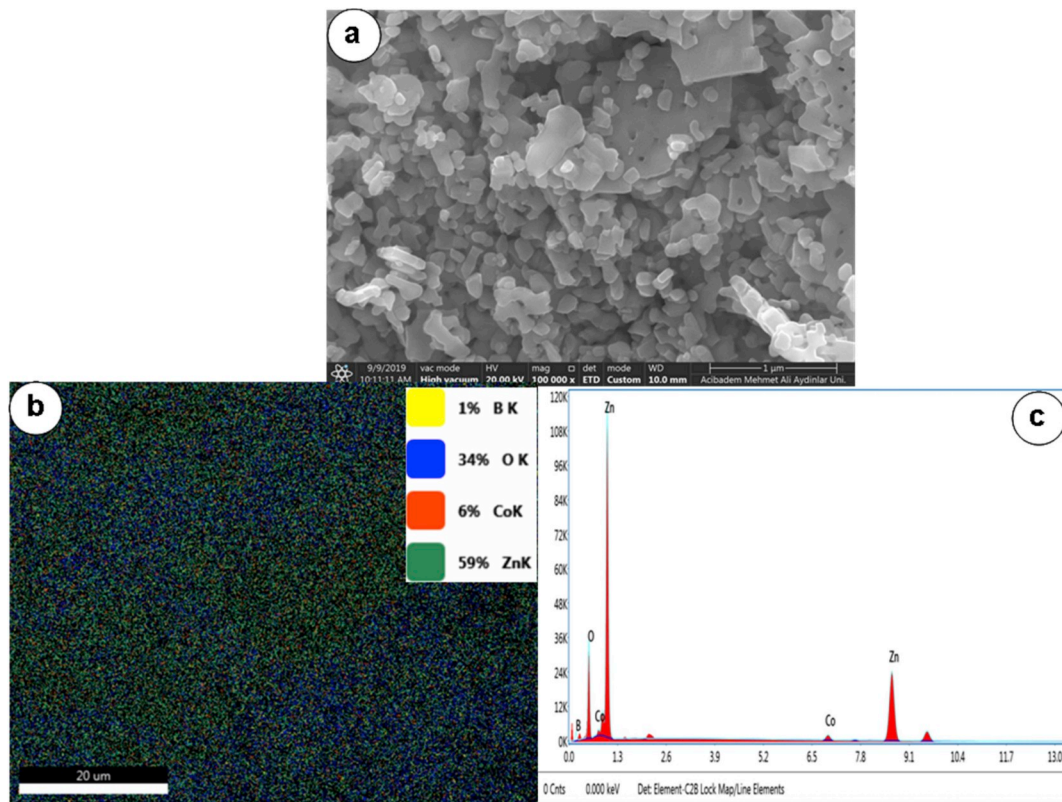


Fig. 10. SEM images of  $Zn_{0.89}Co_{0.04}B_{0.07}O$  composition for 1  $\mu m$  (a), the EDX mapping images (b), and the EDX graph of  $Zn_{0.89}Co_{0.04}B_{0.07}O$  sample in (c).

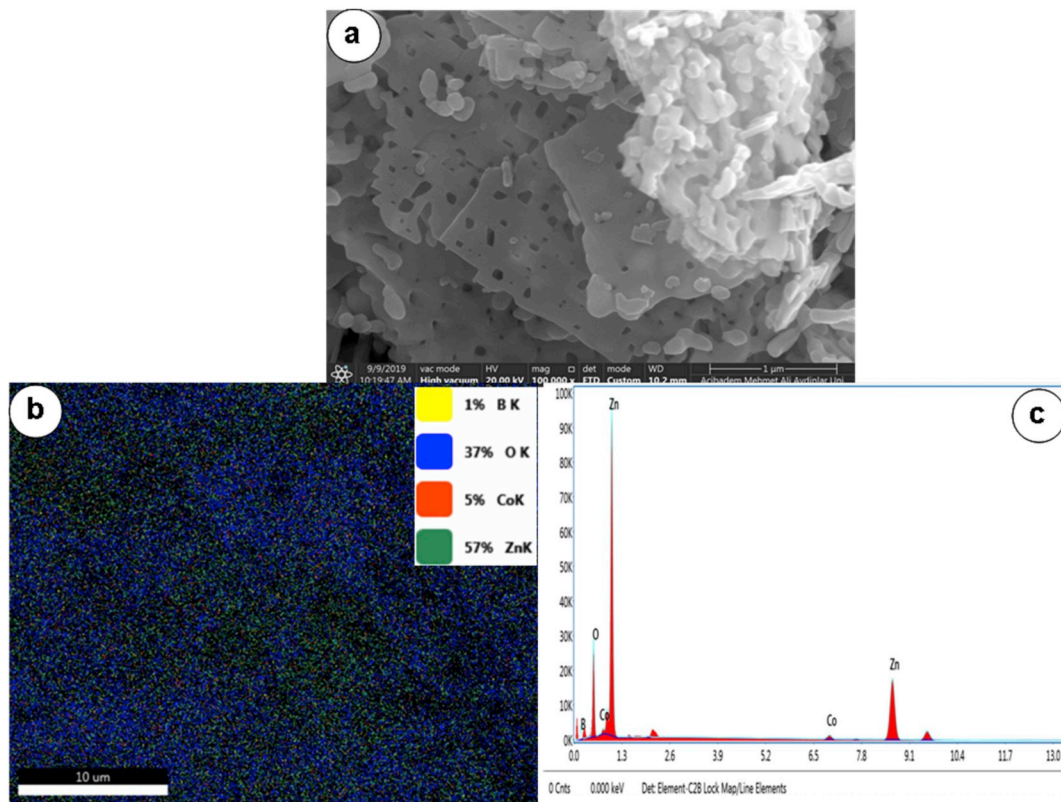


Fig. 11. SEM images of  $Zn_{0.88}Co_{0.05}B_{0.07}O$  composition for 1  $\mu m$  (a), the EDX mapping images (b), and the EDX graph of  $Zn_{0.88}Co_{0.05}B_{0.07}O$  sample in (c).

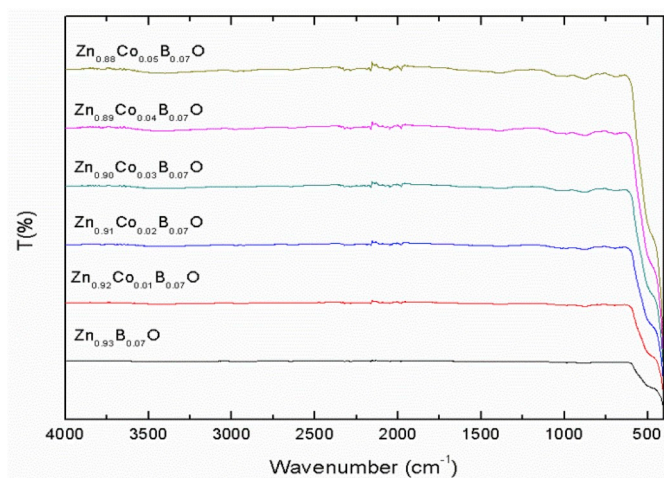


Fig. 12. FTIR spectra of  $Zn_{0.93-x}Co_xB_{0.07}O$  nanoparticles for different Co concentrations from 0% to 5% in the wavenumber range from 450 to 4000  $cm^{-1}$ .

nanoparticles is higher than  $Zn_{0.93-x}Co_xB_{0.07}O$  ( $x = 0.01, 0.02, 0.03, 0.04, 0.05$ ). As shown in Fig. 13, the  $Zn_{0.93}B_{0.07}O$  samples have an absorbance band value at 381.80 nm. This value is consistent with our previous work [41].

The increment of Co concentrations leads to a decrease in absorption and this may be attributed to the created charge carries by Co introduced into Zn–B–O lattice. Moreover, in all cobalt doped ZnBO samples, the spectra include three sub-band absorption bands located at 568, 615 and 659 nm for the Co-doped ZnBO samples. These peaks are related to the d-d transitions of the tetrahedral-coordinated  $Co^{2+}$  ions. The three absorption bands could be attributed to  ${}^4A_2(F) \rightarrow {}^2A_1(G)$ ,  ${}^4A_2(F) \rightarrow {}^4T_1(P)$  and  ${}^4A_2(F) \rightarrow {}^2E(G)$  field transitions, respectively. These observed absorption bands are in good agreement with Co-doped

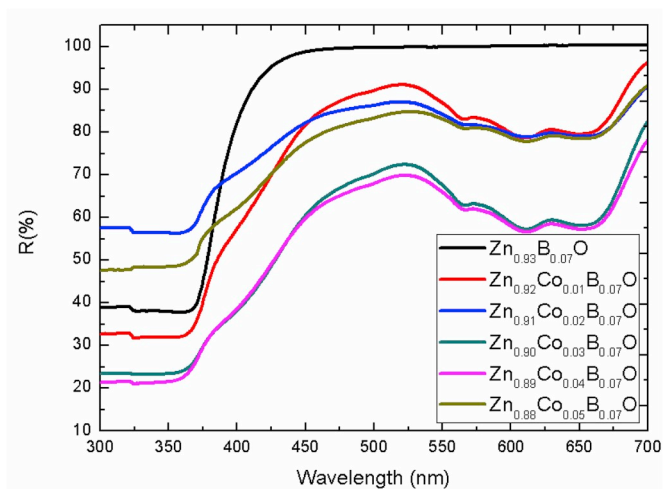


Fig. 13. The reflectance spectra of the  $Zn_{0.93-x}Co_xB_{0.07}O$  ( $x = 0.0, 0.01, 0.02, 0.03, 0.04, 0.05$ ) nanoparticles.

ZnBO nanoparticles by different methods in the literature [57–60].

### 3.4.1. Band gap calculation

The optical band gap  $E_g$  can be determined using the following equation between the absorption coefficient ( $\alpha$ ) and the photon energy ( $h\nu$ ):

$$\alpha h\nu = k(h\nu - E_g)^{1/n} \tag{1}$$

In Eq. (1),  $E_g$  and  $k$  are the optical band gap and energy-independent constants, respectively. Since  $F(R_\infty)$  is proportional to  $\alpha$  and ZnO has direct allowed transitions,  $n$  is taken as 1/2. Thus, Eq. (1) can be transformed to:

**Table 3**  
Fitting curve function  $y(h\nu) = A \times h\nu + B$ , band gap energies, and variances for different Co doping ratios.

Co %	A	B	$E_g$	Relative Error
0.00	25.48	-83.00	3.26	$6.7 \times 10^{-4}$
0.01	34.80	-112.86	3.24	$2.6 \times 10^{-4}$
0.02	1.85	-5.97	3.23	$1.3 \times 10^{-5}$
0.03	81.51	-262.20	3.22	$1.9 \times 10^{-3}$
0.04	109.21	-354.11	3.25	$4.9 \times 10^{-4}$
0.05	3.96	-12.70	3.20	$2.2 \times 10^{-4}$

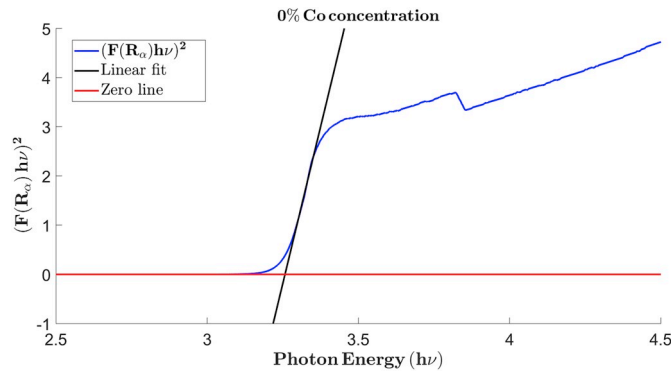


**Fig. 14a.** The plots of  $(F(R_\alpha)h\nu)^2$  as a function of photon energy ( $h\nu$ ) and the linear fit for the  $Zn_{0.93-x}Co_xB_{0.07}O$   $x = 0.00$  nanoparticles, the optical band gap  $E_g = 3.26$  eV.

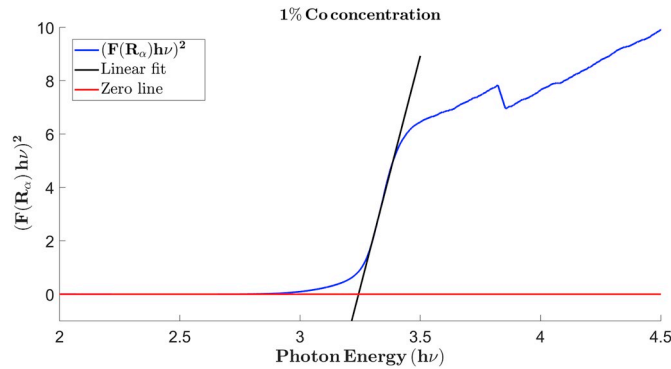


**Fig. 14b.** The plots of  $(F(R_\alpha)h\nu)^2$  as a function of photon energy ( $h\nu$ ) and the linear fit for the  $Zn_{0.93-x}Co_xB_{0.07}O$   $x = 0.01$  nanoparticles, the optical band gap  $E_g = 3.24$  eV.

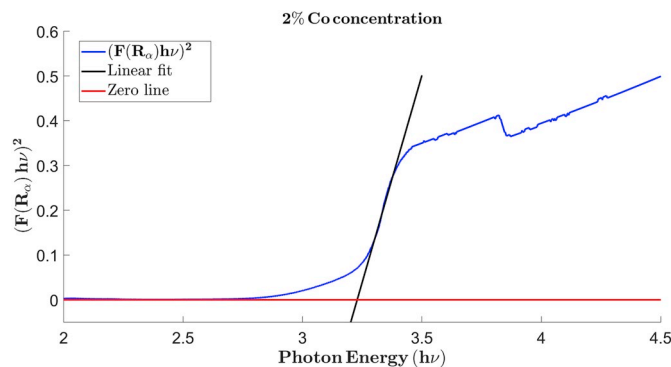


**Fig. 14c.** The plots of  $(F(R_\alpha)h\nu)^2$  as a function of photon energy ( $h\nu$ ) and the linear fit for the  $Zn_{0.93-x}Co_xB_{0.07}O$   $x = 0.02$  nanoparticles, the optical band gap  $E_g = 3.23$  eV.

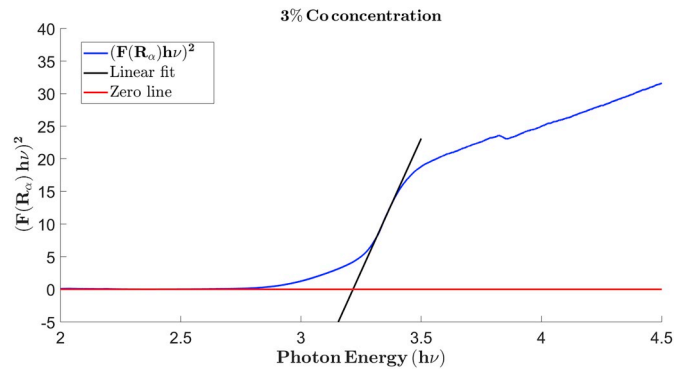


**Fig. 14d.** The plots of  $(F(R_\alpha)h\nu)^2$  as a function of photon energy ( $h\nu$ ) and the linear fit for the  $Zn_{0.93-x}Co_xB_{0.07}O$   $x = 0.03$  nanoparticles, the optical band gap  $E_g = 3.22$  eV.

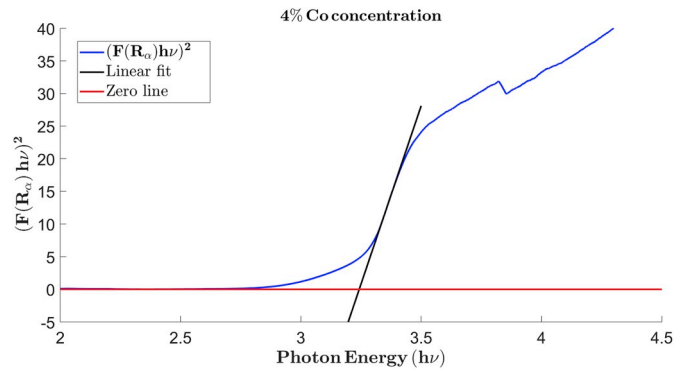


**Fig. 14e.** The plots of  $(F(R_\alpha)h\nu)^2$  as a function of photon energy ( $h\nu$ ) and the linear fit for the  $Zn_{0.93-x}Co_xB_{0.07}O$   $x = 0.04$  nanoparticles, the optical band gap  $E_g = 3.25$  eV.

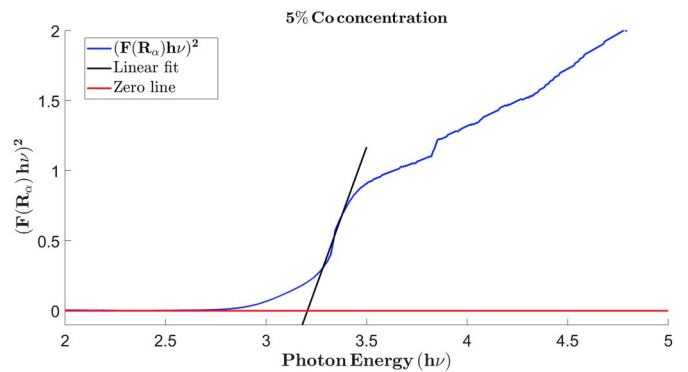


**Fig. 14f.** The plots of  $(F(R_\alpha)h\nu)^2$  as a function of photon energy ( $h\nu$ ) and the linear fit for the  $Zn_{0.93-x}Co_xB_{0.07}O$   $x = 0.05$  nanoparticles, the optical band gap  $E_g = 3.20$  eV.

$$F(R_\alpha) h\nu = k(h\nu - E_g)^{1/2} \tag{2}$$

in other words,  $(F(R_\alpha) h\nu)^2 = k^2(h\nu - E_g)$ . The slope of the graph of  $(F(R_\alpha) h\nu)^2$  was approximated by using a linear fit  $y(h\nu) = A \times h\nu + B$  in the least-squares sense between 350 and 400 nm. To do this, the following error formula given in Eq. (3) was minimized for  $A$  and  $B$

$$E(A, B) = \sum_{i=1}^N [A \times (h\nu)_i + B - ((F(R_\alpha) h\nu)^2)_i]^2 \tag{3}$$

and  $A$ ,  $B$ , the relative error values for these data set were listed in Table 3 where  $N$  is the number of data points.

The band gap energy  $E_g$ , as shown in Table 3 and Figs. 14 a-f, is calculated by the linear approximation of the slope of the graph of

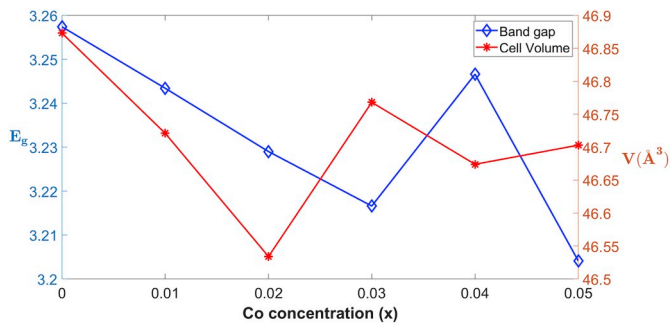


Fig. 15. Concentration-dependent band gap values and cell volume in  $Zn_{0.93-x}Co_xB_{0.07}O$  structures.

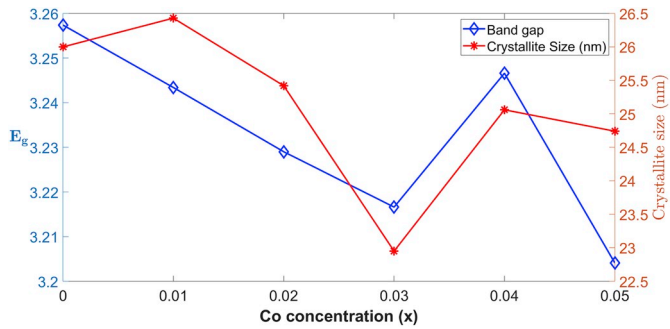


Fig. 16. Concentration-dependent band gap values and particle sizes in  $Zn_{0.93-x}Co_xB_{0.07}O$  structures.

$(F(R_\alpha) h\nu)^2$  to the photon energy axis where  $F(R_\alpha) = 0$ , namely,  $E_g = h\nu = -\frac{B}{A}$ , as plotted in Figs. 14 a-f. In other words, the intersection between the linear fit and the photon energy axis gives the value to  $E_g$ . From Figs. 14 a-f, the band gap energies of the Co/B-doped ZnO nanoparticles samples were observed to be  $3.22 \pm 0.03$  eV. For the  $Zn_{0.93}B_{0.07}O$  sample, the optical energy band gap is found to be about 3.26 eV which is close (3.29 eV) to the reported value in the literature [41]. The band gap energy value is 3.26 eV for  $Zn_{0.93}B_{0.07}O$ ; it decreases to 3.24 eV for  $Zn_{0.92}Co_{0.01}B_{0.07}O$  and to 3.23 eV for  $Zn_{0.91}Co_{0.02}B_{0.07}O$  respectively. The band gap energy became a minimum at 5% Co concentration with a value of 3.20 eV and maximum at 0% Co concentration with a value of 3.26 eV.

As seen in Fig. 15, there is an inverse relationship between the energy band gap and cell volume. The maximum band gap occurs at 0% Co concentration with a value of 3.26 eV and the maximum cell volume occurs at 0% Co concentration with a value of 46.87 Å<sup>3</sup>. Similarly, there is also an inverse relationship between energy band gap and particle size as shown in Fig. 16. The particle size obtained its minimum and maximum at 3% and 1% Co concentrations with the values of 22.95 nm and 26.43 nm, respectively.

### 3.4.2. Refractive index calculation

There has been a great interest in high refractive index  $n$  and wide band gap  $E_g$  because of their applications in optoelectronic and sensor industries. To increase the performance of optical interference filters, optical sensors (e.g. anti-reflection coatings), there is a need not only for the high refractive index but also for wide band gap materials. Lately, Naccarato et al. [1] in 2019 published an article to relate the high refraction index and band gap, they evaluated more than 4000 semiconductors and investigated how the chemistry influences this inverse relationship between refraction index and band gap and rationalized why certain classes of materials would perform better. Naccarato et al. [1] reviewed some of the refractive index calculation models, namely, Ravindra et al. [2], Moss [3], Hervé and Vandamme [4], Reddy and Anjayenulu [5], Kumar and Singh [6].

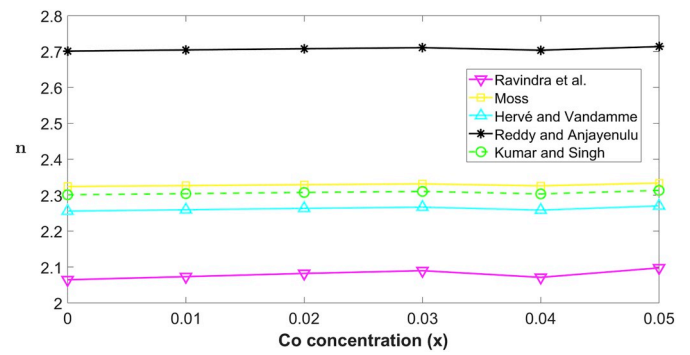


Fig. 17a. Refractive index as a function of Co concentration (x) of  $Zn_{0.93-x}Co_xB_{0.07}O$  structures using all five different models.

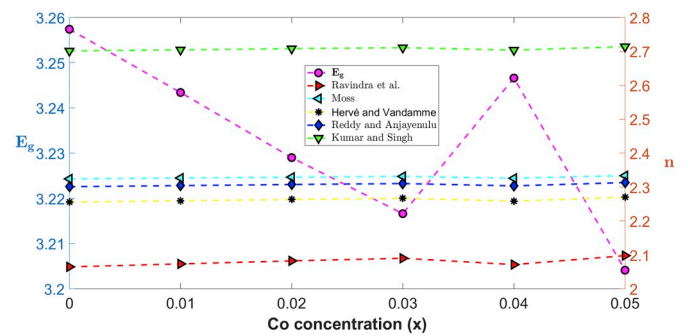


Fig. 17b. Refractive index and band gap as a function of Co concentration (x) of  $Zn_{0.93-x}Co_xB_{0.07}O$  structures using all five different models.

Table 4

Refractive indices calculated by different methods using band gap energies with Co concentration.

%Co concentration	Ravindra et al.	Moss	Hervé and Vandamme	Reddy and Anjayenulu	Kumar and Singh	$E_g$
0	2.06	2.32	2.26	2.70	2.30	3.26
1	2.07	2.33	2.26	2.71	2.30	3.24
2	2.08	2.33	2.26	2.71	2.31	3.23
3	2.09	2.33	2.27	2.71	2.31	3.22
4	2.07	2.33	2.26	2.70	2.30	3.25
5	2.10	2.33	2.27	2.71	2.31	3.20

Fig. 17 a - b exhibited the refractive index varying by Co concentration based on these five models and the calculated values were listed in Table 4. According to the findings of Naccarato et al. [1] (See Fig. 5 therein), our material with ( $n > 2$  and  $E_g > 3$ ) considered in this research is classified as Transition Metals (TMs) with empty  $d$  shell (e.g.  $V^{5+}$ ).

We calculated the refraction index based on the following five models:

Model	Refractive Index ( $n$ ) Formula
Hervé and Vandamme [4]	$\sqrt{1 + \left(\frac{13.6}{E_g + 3.47}\right)^2}$
Kumar and Singh [6]	$3.3668 (E_g)^{-0.32234}$
Moss [3]	$\left(\frac{95}{E_g}\right)^{\frac{1}{4}}$
Ravindra et al. [2]	$4.084 - 0.62 E_g$
Reddy and Anjayenulu [5]	$\left(\frac{154}{E_g - 0.365}\right)^{\frac{1}{4}}$

**Table 5**  
Reliability ranges for the energy band gaps based on the five models.

Model	Reliability Ranges of Band Gaps
Hervé and Vandamme [4]	2.00 eV < $E_g$ < 4.00 eV
Kumar and Singh [6]	2.00 eV < $E_g$ < 4.00 eV
Moss [3]	0.17 eV < $E_g$ < 3.68 eV
Ravindra et al. [2]	1.50 eV < $E_g$ < 3.50 eV
Reddy and Anjayenu [5]	1.10 eV < $E_g$ < 6.20 eV

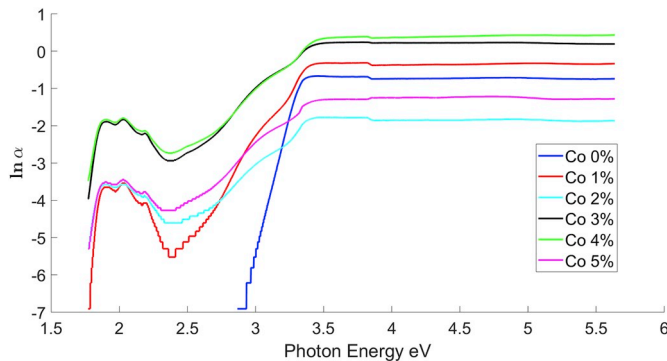


**Fig. 18.**  $\ln \alpha$  versus photon energy (eV) of  $\text{Zn}_{0.93-x}\text{Co}_x\text{B}_{0.07}\text{O}$  structures.

Notice that the high and low refractive indices occurred at Co concentrations 5% and 0%, respectively. As shown in Figs. 17 a - b, the refractive index heavily depends on the Co concentration. The highest refractive index values were obtained at 5% Co doping and the minimum values were obtained at 0% Co doping. In all Figs. 17 a - b, all five models show the same pattern between the energy band gap and refractive index. Among all these five models, Moss and Kumar and Singh give similar results in the range of 2.30–2.34. In 2015, Tripathy [61] gave the following reliability ranges for the energy band gaps based on these five models and these values were listed in Table 5.

As shown in Table 4, our energy band gap values are in the range of 3.20 eV and 3.26 eV, thus refractive index values based on these models are valid.

### 3.4.3. The Urbach energy calculation

In Fig. 18, the logarithm of the absorption coefficient was plotted versus the photon energy eV ( $h\nu$ ) for  $\text{Zn}_{0.93-x}\text{Co}_x\text{B}_{0.07}\text{O}$  structures. The Urbach law states that the absorption coefficient ( $\alpha$ ) near band edges is having an exponential dependence on photon energy ( $h\nu$ ), as given by the following relation:

$$\alpha = \alpha_0 e^{h\nu/E_u}$$

where  $E_u$  is the Urbach energy indicating the effect of all possible

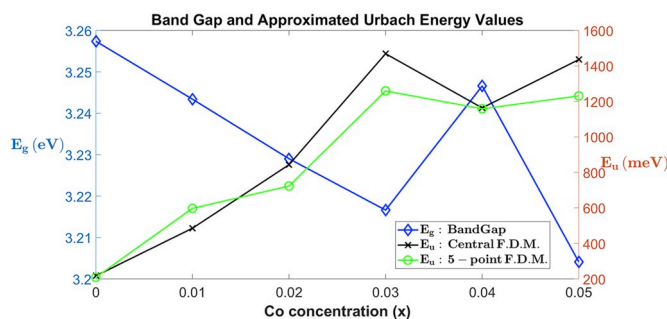


**Fig. 19.** Band gap  $E_g$  as a function of Co concentration ( $x$ ) and Urbach energy ( $E_u$ ) values approximated by two different finite difference methods, namely, 3-point central and 5-point finite difference methods (FDM) of  $\text{Zn}_{0.93-x}\text{Co}_x\text{B}_{0.07}\text{O}$  structures.

**Table 6**  
The Urbach energy values  $E_u$  in meV calculated at  $E_g$  by different finite difference methods (F.D.M.) for the  $\text{Zn}_{0.93-x}\text{Co}_x\text{B}_{0.07}\text{O}$  structures.

% Co concentration	3-point Central F.D.M.	5-point F.D.M.
0	217.42	209.04
1	485.43	597.35
2	843.14	722.69
3	1469.12	1259.04
4	1163.37	1158.27
5	1435.90	1230.78

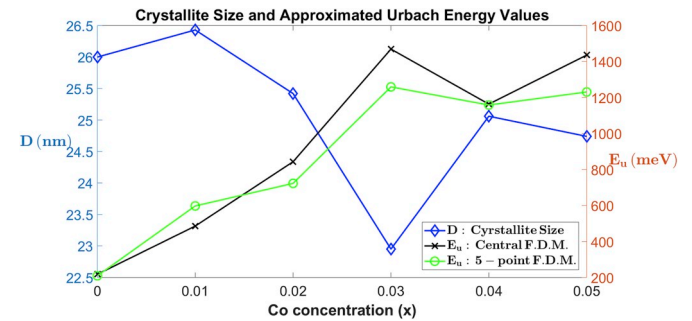


**Fig. 20.** Particle size ( $D$ ) as a function of Co concentration ( $x$ ) and Urbach energy ( $E_u$ ) values approximated by two different finite difference methods, namely, 3-point central and 5-point finite difference methods (FDM) of  $\text{Zn}_{0.93-x}\text{Co}_x\text{B}_{0.07}\text{O}$  structures.

defects and  $\alpha_0$  is a constant [62]. The Urbach energy  $E_u$  values can be related to the width of the localized states in the band gap and are evaluated by using the following relation:

$$E_u = \left[ \frac{d(\ln \alpha)}{d(h\nu)} \right]^{-1}$$

where  $\alpha$  is the absorption coefficient and is the photon energy [63, and the references therein].

However, since we only know the tabulated values of the absorption coefficient, there is a need to approximate the first derivative of  $\ln \alpha$  with respect to the photon energy ( $h\nu$ ). This was done with two different finite difference methods, namely, 3-point central and 5-point formulas. The error in these approximations is of order 2 and 4, respectively. The Urbach energy values  $E_u$  were evaluated at  $h\nu = 3.26$  and plotted in Fig. 19 with band gap values as a function of Co concentration ( $x$ ) of  $\text{Zn}_{0.93-x}\text{Co}_x\text{B}_{0.07}\text{O}$  structures, listed in Table 6. Bindu and Thomas [64] found out that the  $E_u$  value was 490 meV for undoped ZnO nanoparticles. This tells us that doping cobalt increases the Urbach energy value of B-doped ZnO nanoparticles. The increase in  $E_u$  indicates that the structural disorder and the number of defects in the  $\text{Zn}_{0.93-x}\text{Co}_x\text{B}_{0.07}\text{O}$  structures increased with increasing concentration of Co in the  $\text{Zn}_{0.93-x}\text{Co}_x\text{B}_{0.07}\text{O}$  structures. The formation of more interbands in between conduction and valence bands can be explained by the high value of Urbach energy.

The highest value of Urbach energy was approximately found in the range of 1259 and 1469 meV for 3% Co. As shown in Fig. 20 and Table 6, the Urbach energy decreased as the particle size ( $D$ ) increased, signifying a decrement of the structural disorder [64].

## 4. Conclusion

$\text{Zn}_{0.93-x}\text{Co}_x\text{B}_{0.07}\text{O}$  ( $x = 0.00, 0.01, 0.02, 0.03, 0.04, \text{ and } 0.05$ ) nanoparticles were prepared by the hydrothermal method. Its structural, microstructural, and optoelectronic properties were analyzed based on their concentration dependence. The maximum microstrain  $\epsilon$  occurred at  $x = 0.03$ . X-ray diffraction analysis exhibited a single phase of Cobalt and Boron doped ZnO nanoparticles. Moreover, the fluctuations in the

strain and stress values might reveal many physical defects and dislocations in the host lattice structure. The maximum particle size (26.43 nm) occurred at  $x = 0.01$ . At  $x = 0.03$ , dislocation density ( $\delta$ ) had the maximum value of  $1.9 \times 10^{-3}$ . The maximum band gap occurred for  $\text{Zn}_{0.93}\text{B}_{0.07}\text{O}$  with a band gap energy of  $E_g = 3.26$  eV. The highest value of Urbach energy was approximately found in the range of 1259 and 1469 meV for 3% Co. This high value of Urbach energy can explain why the formation of more interbands in between conduction and valence bands occurs.

The grain sizes and the band gap energies fluctuated as the doping ratio increased. It was found that the refractive index strongly depends on the Co concentration. At  $x = 0.00$  and  $x = 0.05$ , the minimum and maximum refractive index values were obtained, respectively.

### Declaration of competing interest

The authors declare that they have no known competing financial interests or personal relationships that could have appeared to influence the work reported in this paper.

### Acknowledgments

This research was supported by the Bolu Abant İzzet Baysal University Scientific Research Projects under the Project No: BAP-2018.03.03.1320, and the Research Fund of Bahcesehir University (BAU-BAP.2018.02.16), Istanbul.

### References

- [1] F. Naccarato, F. Ricci, J. Suntiwich, G. Hautier, L. Wirtz, G.-M. Rignanese, Searching for materials with high refractive index and wide band gap: a first-principles high-throughput study, *Phys. Rev. Mater.* 3 (2019) 044602.
- [2] N.M. Ravindra, S. Auluck, V.K. Srivastava, On the penn gap in semiconductors, *Phys. Status Solidi (b)* 93 (2) (1979) K155–K160.
- [3] T.S. Moss, Relations between the refractive index and energy gap of semiconductors, *Phys. Status Solidi B* 131 (1985) 415.
- [4] P. Hervé, L. Vandamme, General relation between refractive index and energy gap in semiconductors, *Infrared Phys. Technol.* 35 (1994) 609.
- [5] R.R. Reddy, S. Anjaneyulu, Analysis of the Moss and Ravindra relations, *Phys. Status Solidi B* 174 (1992) K91.
- [6] V. Kumar, J. Singh, Model for calculating the refractive index of different materials, *Indian J. Pure Appl. Phys.* 48 (2010) 571.
- [7] S. Noda, M. Fujita, T. Asano, Spontaneous-emission control by photonic crystals and nanocavities, *Nat. Photonics* 1 (2007) 449–458.
- [8] S.P. Hoffmann, M. Albert, N. Weber, D. Sievers, J. Förstner, T. Zentgraf, C. Meier, Tailored UV emission by nonlinear IR excitation from ZnO photonic crystal nanocavities, *ACS Photonics* 5 (5) (2018) 1933–1942.
- [9] C. Ronning, P.X. Gao, Y. Ding, Z.L. Wang, D. Schwen, Manganese-doped ZnO nanobelts for spintronics, *Appl. Phys. Lett.* 84 (2004) 783–785.
- [10] Y.-W. Ra, K.-S. Choi, J.-H. Kim, Y.-B. Hahn, Y.-H. Im, Fabrication of ZnO nanowires using nanoscale spacer lithography for gas sensors, *Small* 4 (2008) 1105–1109.
- [11] Y. Choi, J. Kang, D. Hwang, S. Park, Electron devices, recent advances in ZnO-based light-emitting diodes, *IEEE Trans. Electron Devices* 57 (2010) 26.
- [12] J.B. Webb, D.F. Williams, M. Buchanan, Transparent and highly conductive films of ZnO prepared by refractive magnetron sputtering, *Appl. Phys. Lett.* 39 (1981) 640.
- [13] S.Y. Yurish, *Advances in Microelectronics: Reviews vol. 1*, IFSA Publishing, Barcelona, 2018.
- [14] Z.K. Tang, G.K.L. Wong, P. Yu, M. Kawasaki, A. Ohtomo, H. Koinuma, Y. Segawa, Room-temperature ultraviolet laser emission from self-assembled ZnO micro-particle thin films, *Appl. Phys. Lett.* (72) (1998) 3270–3272 25.
- [15] D.R. Clarke, Varistor ceramics, *J. Am. Ceram. Soc.* 82 (3) (1999) 485–502.
- [16] M.F.M. Noh, N.A. Arzaee, J. Safaei, N.A. Mohamed, H.P. Kim, A.R.M. Yusoff, J. Jang, M.A.M. Teridi, Eliminating oxygen vacancies in SnO<sub>2</sub> films via aerosol-assisted chemical vapor deposition for perovskite solar cells and photoelectrochemical cells, *J. Alloy. Comp.* 773 (2019) 997–1008.
- [17] E. Asikuzun, O. Ozturk, L. Arda, C. Terzioğlu, Preparation, growth and characterization of nonvacuum Cu-doped ZnO thin films, *J. Mol. Struct.* 1165 (2018) 1–7.
- [18] A. Guler, L. Arda, N. Dogan, C. Boyraz, E. Ozugurlu, The annealing effect on microstructure and ESR properties of (Cu/Ni) co-doped ZnO nanoparticles, *Ceram. Int.* 45 (2) (2019) 1737–1745.
- [19] C. Boyraz, N. Dogan, L. Arda, Microstructure and magnetic behavior of (Mg/Ni) co-doped ZnO nanoparticles, *Ceram. Int.* 43 (17) (2017) 15986–15991.
- [20] M. Tosun, L. Arda, Effect of temperature and film thickness on structural and mechanical properties of c-axis oriented Zn<sub>0.95</sub>Mg<sub>0.05</sub>O thin films, *Ceram. Int.* 45 (13) (2019) 16234–16243.
- [21] I.P. Duru, E. Ozugurlu, L. Arda, Size effect on magnetic properties of Zn<sub>0.95-x</sub>Mg<sub>x</sub>Ni<sub>0.05</sub>O nanoparticles by Monte Carlo simulation, *Ceram. Int.* 45 (2019) 5259–5265.
- [22] S.D. Senol, C. Boyraz, E. Ozugurlu, A. Gungor, L. Arda, Band gap engineering of Mg doped ZnO nanorods prepared by a hydrothermal method, *Cryst. Res. Technol.* 54 (3) (2019) 1800233.
- [23] D. Akcan, S. Ozharar, E. Ozugurlu, L. Arda, The effects of Co/Cu Co-doped ZnO thin films: an optical study, *J. Alloy. Comp.* 797 (2019) 253–261.
- [24] N. Doğan, A. Bingölbali, L. Arda, Preparation, structure and magnetic characterization of Ni-doped ZnO nanoparticles, *J. Magn. Magn. Mater.* 373 (2015) 226–230.
- [25] E. Asikuzun, O. Ozturk, L. Arda, C. Terzioğlu, Microstructural and electrical characterizations of transparent Er-doped ZnO nano-thin films prepared by sol-gel process, *J. Mater. Sci. Mater. Electron.* 28 (2017) 14314–14322.
- [26] L. Arda, The effects of Tb doped ZnO nanorod: an EPR study, *J. Magn. Magn. Mater.* 475 (2019) 493–501.
- [27] U. Ozgur, Y.I. Alivov, C. Liu, A. Teke, M.A. Reshchikov, S. Dogan, V. Avrutin, S.J. Cho, H. Morkoc, A comprehensive review of ZnO materials and devices, *J. Appl. Phys.* 98 (2005) 041301.
- [28] Z.K. Heiba, L. Arda, M.B. Mohamed, N.Y. Mostafa, M.A. Al-Jalali, N. Dogan, Effect of annealing temperature on structural and magnetic properties of Zn<sub>0.94</sub>Co<sub>0.05</sub>Cu<sub>0.01</sub>O, *J. Supercond. Nov. Magnetism* 26 (2013) 3299–3304.
- [29] T. Pandiyarajan, R. Udayabhaskar, B. Karthikeyan, Role of Fe doping on structural and vibrational properties of ZnO nanostructures, *Appl. Phys. A* 107 (2012) 411–419.
- [30] G.H. Mhlongo, K. Shingange, Z.P. Tshabalala, B.P. Dhonge, F.A. Mahmoud, B.W. Mwakikunga, D.E. Motaung, Room-temperature ferromagnetism and gas sensing in ZnO nanostructures: influence of intrinsic defects and Mn Co, Cu doping, *Appl. Surf. Sci.* 390 (2016) 804–815.
- [31] H.T. Cao, Z.L. Pei, J. Gong, C. Sun, R.F. Huang, L.S. Wen, Preparation and characterization of Al and Co-doped ZnO (ZnO:(Al, Co)) transparent conducting oxide films, *J. Solid State Chem.* 177 (2004) 1480.
- [32] N. Bahadur, A.K. Srivastava, S. Kumar, M. Deepa, B. Nag, Influence of cobalt doping on the crystalline structure, optical and mechanical properties of ZnO thin films, *Thin Solid Films* 518 (2010) 5257.
- [33] F. Ahmed, S. Kumar, N. Arshi, M.S. Anwar, B.H. Koo, C.G. Lee, Doping effects of Co<sup>2+</sup> ions on structural and magnetic properties of ZnO nanoparticles, *Microelectron. Eng.* 89 (2012) 129–132.
- [34] Z.K. Heiba, L. Arda, XRD, XPS, optical, and Raman investigations of structural changes of nano Co-doped ZnO, *J. Mol. Struct.* 1022 (2012) 167–171.
- [35] R. Siddheswaran, R.V. Mangalaraja, R.E. Avila, D. Manikandan, C. Esther Jayanthi, S. Ananthakumar, Evaluation of mechanical hardness and fracture toughness of Co and Al co-doped ZnO, *Mater. Sci. Eng. A* 558 (2012) 456–461.
- [36] L. Arda, M. Acikgoz, N. Dogan, D. Akcan, O. Cakiroglu, Synthesis, characterization and ESR studies of Zn<sub>1-x</sub>Co<sub>x</sub>O nanoparticles, *J. Supercond. Nov. Magnetism* 27 (2013) 799–804.
- [37] E. Asikuzun, A. Donmez, L. Arda, O. Cakiroglu, D. Akcan, O. Ozturk, M. Tosun, S. Ataoglu, C. Terzioğlu, Structural and mechanical properties of (Co/Mg) co-doped nano ZnO, *Ceram. Int.* 41 (2015) 6326–6334.
- [38] L. Gao, Y. Zhang, J.M. Zhang, K.W. Xu, Boron doped ZnO thin films fabricated by RF-magnetron sputtering, *Appl. Surf. Sci.* 257 (7) (2011) 2498–2502.
- [39] A.J. Reddy, M.K. Kokila, H. Nagabhushan, R.P.S. Chakradhar, C. Shivakumar, J.L. Rao, B.M. Nagabhushan, Structural, optical and EPR studies on ZnO: B nanoparticles prepared via low-temperature solution combustion synthesis, *J. Alloy. Comp.* 509 (2011) 5349–5355.
- [40] S. Muthukumaran, R. Gopalakrishnan, Structural, FTIR and photoluminescence studies of B doped ZnO nanopowders by co-precipitation method, *Opt. Mater.* 34 (2012) 1946–1953.
- [41] S.D. Senol, O. Ozturk, C. Terzioğlu, Effect of boron doping on the structural, optical and electrical properties of ZnO nanoparticles produced by the hydrothermal method, *Ceram. Int.* 41 (9) (2015) 11194–11201 Part A.
- [42] B. Wen, C.Q. Liu, N. Wang, H.L. Wang, S.M. Liu, W.W. Jiang, W.Y. Ding, W.D. Fei, W.P. Chai, Properties of boron-doped ZnO thin films deposited by pulsed DC magnetron sputtering at different substrate temperatures, *Appl. Phys. A* 121 (2015) 1147–1153.
- [43] Yang Jin, Jian Huang, Huanhuan Ji, Ke Tang, Lei Zhang, Bing Ren, Meng Cao, Linjun Wang, Effect of RF power and substrate temperature on the properties of boron and gallium co-doped ZnO films, *Mater. Sci. Semicond. Process.* 53 (2016) 84–88.
- [44] J. Steinhäuser, S. Fay, N. Oliveria, Transition between grain boundary and intragrain scattering transport mechanisms in boron-doped zinc oxide thin films, *Appl. Phys. Lett.* 90 (2007) 142107.
- [45] C.Y. Tsay, W.T. Hsu, Sol-gel derived undoped and boron-doped ZnO semiconductor thin films: preparation and characterization, *Ceram. Int.* 39 (2013) 7425–7432.
- [46] B.K. Shin, T.I. Lee, J.H. Park, et al., Preparation of Ga-doped ZnO films by pulsed dc magnetron sputtering with a cylindrical rotating target for thin film solar cell applications, *Appl. Surf. Sci.* 258 (2011) 834–838.
- [47] V. Kumar, F. Singh, O.M. Ntwaeaborwa, H.C. Swart, Effect of Br<sup>+</sup> ions on the structural, morphological and luminescent properties of ZnO/Si thin films, *Appl. Surf. Sci.* 279 (2013) 472–478.
- [48] K. Ellmer, Resistivity of polycrystalline zinc oxide films: current status and physical limit, *J. Phys. D Appl. Phys.* 34 (2001) 3097.
- [49] B.N. Pawar, S.R. Jadhav, M.G. Takwale, Preparation of transparent and conducting boron-doped ZnO electrode for its application in dye-sensitized solar cells, *J. Phys. Chem. Solids* 66 (2005) 1779.
- [50] S. Kim, H. Park, G. Nam, H. Yoon, J. Su Kim, J.S. Kim, J.-S. Son, S.-H. Lee, J.-Y. Leem, Temperature-dependent photoluminescence of boron-doped ZnO nanorods, *Bull. Korean Chem. Soc.* 34 (11) (2013) 3335.
- [51] R.B.H. Tahar, N.B.H. Tahar, Boron-doped zinc oxide thin films prepared by sol-gel

- technique, *J. Mater. Sci.* 40 (2005) 5285–5289.
- [52] S. Jana, A.S. Vuk, A. Mallick, B. Orel, P.K. Biswas, Effect of boron doping on optical properties of sol–gel based nanostructured zinc oxide films on glass, *Mater. Res. Bull.* 46 (2011) 2392–2397.
- [53] K. Vanheusden, W.L. Warren, C.H. Seager, D.R. Tallant, J.A. Voigt, B.E. Gnade, Mechanisms behind green photoluminescence in ZnO phosphor powders, *Appl. Phys.* 79 (1996) 7983–7990.
- [54] M. Andres-Vergés, A. Mifsud, C.J. Serna, Formation of rod-like zinc oxide microcrystals in homogeneous solutions, *J. Chem. Soc., Faraday Trans.* 86 (1990) 959–963.
- [55] X. Sui, Y. Liu, C. Shao, Y. Liu, C. Xu, Structural and photoluminescent properties of ZnO hexagonal nano prisms synthesized by microemulsion with polyvinyl pyrrolidone served as surfactant and passivant, *Chem. Phys. Lett.* 424 (2006) 340–344.
- [56] S.K. Kansal, A.H. Ali, S. Kapoor, D.W. Bahnemann, Synthesis of flower-like zinc oxide nanostructure and its application as a photocatalyst, *Separ. Purif. Technol.* 80 (2011) 125–130.
- [57] J. Li, L. Zhang, J. Zhu, W. Hao, Aligned ZnO: Co nanorod arrays: electrophoretic deposition fabrication and magnetic manipulation, *Ceram. Int.* 41 (2015) 3456–3460.
- [58] R. He, B. Tan, C. Ton-Hhat, M. Phillips, T. Tsuzuki, Physical structure and optical properties of Co-doped ZnO nanoparticles prepared by co-precipitation, *J. Nanoparticle Res.* 15 (2013) 2030.
- [59] M. Shatnawi, A.M. Alsmadi, I. Bsoul, B. Salameh, G.A. Alna'washi, F. Al-Dweri, F. El Akkad, Magnetic and optical properties of Co-doped ZnO nanocrystalline particles, *J. Alloy. Comp.* 655 (2016) 244–252.
- [60] H. Ji, C. Cai, S. Zhou, W. Liu, Structure, photoluminescence, and magnetic properties of Co-doped ZnO nanoparticles, *J. Mater. Sci. Mater. Electron.* 29 (2018) 12917–12926.
- [61] S. Tripathy, Refractive indices of semiconductors from energy gaps, *Opt. Mater.* 46 (2015) 240–246.
- [62] H. He, F. Zhuge, Z. Ye, L. Zhu, F. Wang, B. Zhao, J. Huang, Strain and its effect on optical properties of Al-N codoped ZnO films, *J. Appl. Phys.* 99 (2006) 023503.
- [63] R. Vettumperumal, S. Kalyanaraman, B. Santoshkumar, R. Thangavel, Estimation of electron-phonon coupling and Urbach energy in group-I elements doped ZnO nanoparticles and thin films by sol-gel method, *Mater. Res. Bull.* 77 (2016) 101–110.
- [64] P. Bindu, S. Thomas, Optical properties of ZnO nanoparticles synthesized from a polysaccharide and ZnCl<sub>2</sub>, *Acta Phys. Pol. A* 131 (2017) 1474–1478.